Sensors and Materials, Vol. 17, No. 6 (2005) 317–333
MYU Tokyo

S & M 0610

Locating and Tracking the Evolution of Debonds at the Interface of Bonded Semiconductor Devices Using Infrared Photoelasticity

Gavin Horn*, Thomas J. Mackin and Jon Lesniak[1]

University of Illinois at Urbana-Champaign,
Department of Mechanical and Industrial Engineering,
1206 West Green Street, Urbana, IL 61802, USA

[1]Stress Photonics, Inc., 3002 Progress Road, Madison, WI 53716, USA

(Received December 9, 2004; accepted May 13, 2005)

Key words: bonded silicon, defect detection, infrared photoelasticity, bond defects, wafer bonding, nondestructive evaluation

An infrared grey-field polariscope (IR-GFP) was developed as a new tool to reliably detect small defects at bonded interfaces and to distinguish between trapped interfacial defects. The IR-GFP improves upon infrared transmission (IRT) imaging by measuring the stress-fields associated with defects. The IR-GFP was validated using anodically bonded glass-silicon samples followed by imaging interface defects in fusion bonded silicon wafer pairs. Defect maps collected using the IR-GFP were contrasted with defect maps collected using conventional IRT imaging, showing that the IR-GFP has improved defect resolution. In addition, because the IR-GFP measures the defect stress field, it can distinguish between trapped gas and trapped particle defects. Furthermore, by imaging the residual stress signature associated with defects, the IR-GFP can detect defects smaller than the wavelength of the transmitted near IR (1.1 micron). Finally, utilizing the residual stress signature associated with trapped gas defects, the IR-GFP was used to track the evolution of time-dependent gas bubbles during annealing of fusion-bonded wafer pairs.

1. Introduction

Wafer bonding processes are susceptible to two key defects at the bonded interface: (i) trapped gases and (ii) contaminant particles.[(1)] It is well understood that both defects generate a local debond that affects the mechanical integrity of the device. However, each defect also generates a local stress state with a magnitude depending on the bonding method, defect dimensions, defect type, and internal gas pressure. Gasses may by trapped by initiation of multiple bond fronts at several locations along the interface, or by local dimensional mismatch.[(2,3)] Most commercial bonders have mitigated these problems by

*Corresponding author, e-mail address: ghorn@uiuc.edu

bonding under vacuum conditions and by utilizing special fixtures designed to initiate a single bond front from a central contact point. Yet, even with such care it has proven nearly impossible to eliminate all trapped gas defects at the bonded interface.

If trapped gas bubbles can be located early in the fabrication process, it may be possible to sort wafers prior to further processing in order to improve process yields. Traditional infrared transmission (IRT) imaging is diffraction limited and, in many cases, falls short of the resolution limits imposed by the industry trend toward further miniaturization. It is known that IRT imaging cannot detect many of the smallest defects that appear at bonded interfaces, yet no existing inspection technology can present results as rapidly.[1] In this paper, we discuss the application of a recently developed automated, infrared grey-field polariscope as a rapid tool for locating trapped gas bubbles with improved resolution compared to IRT imaging. A similar study focusing on particle contamination is presented in a separate paper.[4]

In addition to the need for early detection of gas bubbles at bonded interfaces, there is the challenge of understanding how these defects evolve throughout the bonding process. The traditional fusion bonding process generally consists of three steps: 1) wafer surface preparation, 2) initial bonding at room temperature, and 3) annealing to increase bond strength. Several researchers have reported that wafer pairs that appear defect free after the second step may develop bubbles early in the third step, and these defects may eventually disappear after long annealing times. These defects are often called "time-dependent bubbles." Shimbo *et al.*[5] first reported this phenomenon using infrared transmission inspection and proposed that the voids that formed during annealing at 500°C were attributed to water released from the interface. The voids disappeared when samples were annealed at temperatures above 1000°C, which Shimbo *et al.* attributed to an increased surface oxidation rate. Abe *et al.*[6] speculated that vaporized water caused bubble formation and is the gas trapped in the bubbles, while Mitani *et al.*[7] suggested the presence of hydrocarbons is necessary to nucleate bubbles and that hydrogen from trapped water contributes to the further growth of these bubbles. However, Mack *et al.*[8] found gasses trapped in cavities to consist mostly of H_2, H_2O, and N_2, with only occasional trace amounts of hydrocarbons. Ayón *et al.*[9] recently carried out an experimental characterization of these bubbles using IRT imaging and transmission electron microscopy. While the exact mechanism for bubble formation and growth during annealing is not generally agreed upon, it is apparent that high trapped pressures may occur.[8] The resulting residual stresses can be large enough to cause failure of the substrate wafers.[9]

It is important to note that in each of these investigations, the authors appear to determine that the interface was "defect free" prior to annealing on the basis of the results of wafer-scale IRT imaging. However, the limited defect resolution of IRT is further decreased when inspecting an entire wafer with a single exposure. It is possible that some small defects were present, but undetected. For example, the results from one study[9] display circular distributions of time dependent bubbles attributed to mechanical spacers. Three circular spacers hold the wafers apart while they are being contacted at a central location. While retracting these spacers during bonding, it is likely that contaminants were left behind, generating localized debonds on the surface. These debonds may be too small to locate with IRT initially, but would likely provide initiation sites for the trapped gases to

accumulate during subsequent annealing.

The recently introduced infrared grey-field polariscope (IR-GFP) is an instrument for rapidly measuring in-plane shear stresses in thin silicon and other semiconductor materials.[10] This tool has been used by the authors to locate trapped particles in adhesively,[11] anodically[4] and fusion-[4]bonded devices. In each case, the IR-GFP located defects that were too small to detect by IRT imaging. Furthermore, these defects were successfully located in bonded pairs fabricated with both double-side-polished and single-side-polished wafers. In adhesively bonded devices, the IR-GFP was able to distinguish between trapped particles and gas bubbles because each defect generated significantly different residual stress signatures in the silicon substrates. Even though the IRT signatures of trapped gasses and particles appeared similar, there was no IR-GFP stress signature associated with the gasses trapped completely in the adhesive layer. However, gas bubbles trapped in anodically and fusion-bonded devices are expected to generate significant residual stresses. In this paper, we show that the IR-GFP is capable of locating trapped gas bubbles at the interface of bonded silicon devices which were not apparent using IRT imaging and that it is also capable of differentiating these bubbles from trapped particles. We further show that this tool can track the evolution of debonds during annealing stages of fusion-bonded silicon wafers.

2. Imaging Defects

2.1 *Current imaging technologies*

Infrared transmission imaging is the most common method of inspecting bonded silicon devices. Other techniques, such as scanning acoustic microscopy and X-ray topography have been implemented in the past, but have important limitations for many common applications.[12] A conventional IRT system, schematically illustrated in Fig. 1(a), has two basic components; 1) an infrared light source, and 2) an infrared detector.[i] Depending upon the target material and the material thickness, a significant portion of the projected IR light is transmitted, but partial reflections are encountered at each air-silicon interface. As such, in regions where trapped gas, particles or dimensional mismatch cause local debonds, a portion of the light is doubly reflected by these internal surfaces, generating an interference pattern known as Newton's rings, Fig. 2. By counting the number of Newton's rings at the location of each defect, it is possible to determine the height of the debond. Defects with an opening displacement less than half the illuminating wavelength of light, approximately 0.55 μm for near IR, will not generate a full set of Newton's rings. Debonds thinner than 0.28 μm will cause less than half a set of rings to form, precluding the use of Newton's rings to detect these defects. In some cases, it is possible to qualitatively locate these thin debonds by carefully measuring the shift in optical density caused by the interference. Such defects are considered subfringe because the interference is not capable of producing a single Fizeau fringe. Two subfringe defects can be seen directly to the right of the Newton's ring defect in Fig. 2.

IRT is limited by the operator's ability to resolve distinct fringes and the minimum wavelength of light that can be transmitted. Also, identical Newton's rings form around both trapped particles and gas bubbles making them impossible to differentiate. Further-

[i]Detectors can be anything from an expensive military-grade InGaAs near-IR CCD camera to a traditional Vidicon detector to modern affordable silicon CCD cameras.

more, it is often difficult to determine the full extent of the debond region because the optical density change associated with a defect gradually decays to zero as the optical path length decreases. In other words, the edge of the last Newton's ring does not coincide with the edge of the debond. When bonding single side polished wafers, the rough outer surface is known to greatly decrease the signal-to-noise ratios in IRT imaging.[12] Finally, a faint four-lobed "blooming" pattern is sometimes detected in the IRT images collected using the current embodiment of the IR-GFP with a silicon CCD. This problem has been resolved by utilizing cameras optimized for NIR. Although this pattern is distracting, it does not hinder detection of Newton's ring as shown in Fig. 2.

Other common bond inspection techniques include X-ray topography (XRT) and scanning acoustic microscopy (SAM).[1] The typical spatial resolution of XRT is on the order 2–20 μm, while the spatial resolution of SAM is on the order of 10 μm. As such, these techniques are well suited for detecting small interface defects. These techniques suffer, however, from being significantly more expensive, time consuming and operator intensive. For example, several hours are needed to inspect an entire four-inch bonded wafer pair by XRT.[1] Although SAM is more rapid than XRT, it is significantly slower than IRT because a single data point is collected at each scan location compared with the full-field data collected using the array-based detectors typical of IRT (*e.g.*, 320×320 or 480×640). Even though XRT and SAM provide improved resolution, their speed, cost, and potential incompatibility with cleanroom processing[12] generally restrict these techniques from being amenable to distributed in-line inspection.

2.2 *Infrared photoelasticity*

To overcome the limitations of infrared transmission imaging, an infrared grey-field polariscope was developed and utilized in this study. This tool is an extension of the visible-light grey-field polariscope, which has proven to be successful in measuring residual shear stresses in a host of glass applications.[13] A grey-field polariscope is best described as a fusion between a circular and a plane polariscope, Fig. 1(b). A circularly polarized light projector is built by placing a condenser lens, a polarizer, and a quarter-wave plate between the infrared light source and the sample. A simple linear polarizer is

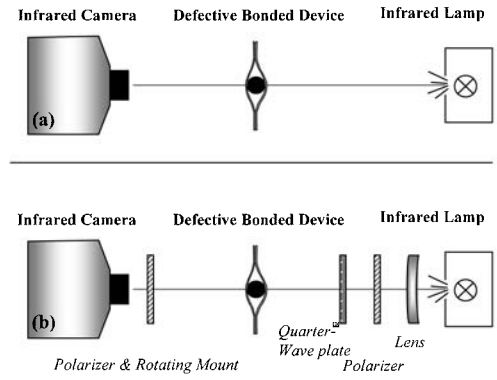

Fig. 1. Standard instrument layout. (a) infrared transmission imaging (b) infrared grey-field polariscope.

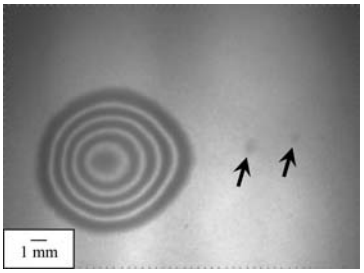

Fig. 2. IRT image of bonded wafer device, showing Newton's ring pattern associated with interfacial defect.

placed in front of a near-IR silicon CCD camera as in a plane polariscope; however, in this implementation, the polarizer is mounted in a rotating stage. These modifications transform the infrared transmission apparatus into an infrared polariscope that is highly sensitive to very small changes in residual stress state. A detailed description of the visible light embodiment of the device is contained in ref. 14, while the implementation using infrared wavelengths is described in ref. 10.

A bonded sample is placed between the circularly polarized illuminator and the analyzer. In the absence of stress in the bonded sample, the transmitted light retains its circular polarization. Stress induced birefringence in the silicon sample will alter the polarization of the light. The component of light propagating along the slow axis is retarded by a phase lag, Δ, with respect to light propagating along the fast axis of the sample as given by

$$\Delta = \frac{2\pi C d}{\lambda}\left(\sigma_1 - \sigma_2\right) \tag{1}$$

where d is the material thickness, λ is the wavelength of light, C is the stress optic coefficient of the material, and σ_1 and σ_2 are the first and second principal stresses. In regions where defects are trapped at the bond interface, residual stresses are present and the transmitted light becomes elliptically polarized in proportion to the magnitude of the stress. Elliptically polarized light that is analyzed with a rotating polarizer will produce a sinusoidally varying light intensity at the camera. The amplitude and phase of this sine wave are determined and the magnitude of the in-plane shear stress and direction of the principal stresses are quantified. With this algorithm, the IR-GFP will only capture sinusoidally varying light intensity that is in phase with the rotating polarizer. As such, the "blooming" pattern is not as prevalent in the IR-GFP stress images captured simultaneously with the IRT images. By employing signal processing outlined in ref. 10 and eq. (1), the IR-GFP calculates the $(\sigma_x - \sigma_y)$ component of stress. A full field residual stress image can be collected in approximately 10 s. IRT images are simultaneously captured by averaging the total light intensity reaching the camera over a full revolution of the polarizer.

3. Locating Defects Generated During Initial Bonding

3.1 *Anodically bonded glass-silicon samples*

Initial experiments were conducted on anodically bonded glass-silicon samples to enable light microscopy through the glass layer. The silicon substrates were fabricated from 525-μm-thick, P-doped (100) silicon wafers. Square 20 mm dice were released from the wafer with an inductively coupled plasma deep reactive ion etching (ICP-DRIE) tool. In some of these dice, cavities and channels were simultaneously etched to a depth of approximately 100 μm for a separate investigation. Pyrex #7740 wafers measuring 525 μm thick were diced for the glass half of the anodically bonded couple. Both substrates were rinsed with acetone and isopropyl alcohol then dried with nitrogen prior to bonding, but rigorous cleaning was intentionally not performed. Many of the defects identified here could have been eliminated with additional RCA cleaning; however, for this investigation, the wide range of defect initiation sites left on the surfaces was used to explore the capabilities of the device. Substrates were anodically bonded in an EVG501 wafer bonding system, where the sample stack was heated to 450°C in a 5×10^{-3} mbar vacuum. The electrode applies 80 N of clamping force to the sample stack and a 500 V potential for 5 min.

3.1.1 *Results for double-side-polished Silicon Wafer*

As a result of the minimal cleaning procedure, several anodically bonded samples had large defect populations. Figures 3(a) and 3(b) show typical IRT and IR-GFP images of an anodically bonded glass-silicon sandwich, populated with both particle-supported and gas-supported debonds along the interface. The typical residual stress signature associated with trapped particles is highlighted by the arrow labeled as ‘a, ’ where a “bow-tie” pattern is centered over the particle.[4] A radially symmetric stress pattern is generated by this defect geometry. This stress pattern appears as a four-lobed “bow-tie” geometry with alternating regions of positive (black) and negative (white) shear in the stress images generated by the IR-GFP. This pattern is analogous to the dark-field photoelastic patterns collected during glass indentation[15] as discussed in ref. 16. The residual stress signature associated with particle defects arises from a combined contact and bending stress field that displays a large residual stress pattern at the central portion of the defect, which decays as 1/r.[16] Trapped-particle stress fields will generally involve a superposition of two signatures, as the opening force of the trapped particle will create both a contact stress field and a loaded-plate stress field at the bond front. However, both stress fields are often not distinguishable when the debond radius is smaller than the extent of the contact stress field.

The IR-GFP signature associated with the other interfacial defects shows a stress concentration at the bond front with little to no measurable residual stress within the debond region itself (for example, see arrow ‘b’ in Fig. 3). This pattern matches the elasticity solution for a circularly clamped plate with a distributed pressure, which provides a good model for a trapped bas bubble. There are distinct differences between the two defects: one is characterized by a contact stress field, the other by a pressurized-plate stress

field, allowing distinction between defect types in bonded devices. Several other optical density variations are noted in the IRT image (such as arrow 'c') that are due to surface contamination. The presence of these defects on the outer surface does not generate a residual stress and does not confound the IR-GFP shear stress images.

Though many of the larger gas bubble defects are readily seen using IRT imaging (Fig. 3(a)), none of these defects has a significant enough opening displacement to create a full set of Newton's rings. More importantly, there are several locations (highlighted by the horizontal black arrows in Fig. 3(b)) where the localized residual stress state measured using the IR-GFP has no counterpart in the IRT images. Figure 3(c) shows the same sample inspected through the glass side at twice the magnification using visible light microscopy. This image verifies that the three defect locations indicated by the horizontal black arrows are debond regions that are not supported by trapped particles. The most important result from inspection of anodically bonded samples is that there is a one-to-one correspondence between the residual stress patterns located using the IR-GFP and trapped-particle/gas defects observed using visible light microscopy. Furthermore, as with trapped particles, the IR-GFP is again capable of detecting defects that are smaller than those

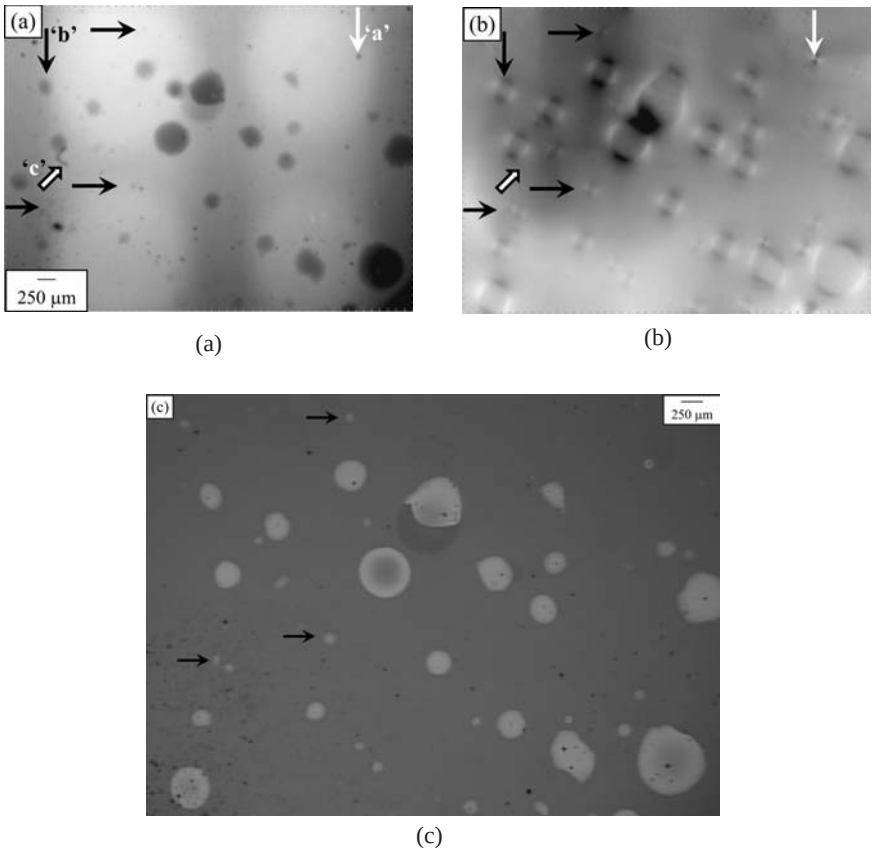

(a) (b)

(c)

Fig. 3. Anodically bonded sample with trapped gas bubbles. (a) IRT image and (b) shear stress image from IR-GFP; (c) visible-light reflection microscopy.

detected by IRT imaging.

The minimum defect resolution has not yet been quantified at this point in the development of the IR-GFP. With this technique, debonds are detected by sensing the residual stress generated by the defects, so the resolution of this system depends on the magnitude of this stress. As such, the minimum defect size will depend on several material and processing properties. For example, it will be easier to locate smaller particles when using bonding techniques with higher bond energies and stiffer substrates (and stiffer particles), because this combination will lead to high contact stresses. In addition, the detection limit is also strongly dependent upon the stress optic coefficient of the material inspected. Larger values of C will generate more retardation for the same level of stress, allowing detection of smaller defects. As a minimum debond size has not been sought and these samples were not inspected by either SAM or XRT, it is difficult to compare these techniques. However, IR-GFP imaging can locate debonds measuring less than 10 μm at 5–10× lower magnification than required by IRT imaging.[16] As such, it is anticipated that the IR-GFP will have a resolution similar to those of SAM and XRT, while collecting data at significantly higher rates.

In many cases, trapped-gas defects also contain particles within their boundaries. Figures 4(a)–4(c) show several such defects along the left side of the image. As noted earlier, if these particles support a load in these defects, a concentrated "bow-tie" signature will be found. Debonds supported only by trapped gasses will not display this concentrated stress. However, some defects may be supported by a combination of particle contact and gas pressure. These defects can be found by a faint bow-tie pattern surrounded by a strong stress field at the bond front, or a bow-tie pattern that is not located at the center of a debond. A small defect at the lower left corner of the image shows two particles within the defect, one which has a faint contact stress field (black arrow), the other which shows no stress (white arrow), indicating that this latter particle is freely floating within the defect. A strong stress concentration surrounds these particles at the bond front, indicating that although one particle carries some load, there is significant support from trapped gas pressure. Another defect near the center of the left side shows a trapped particle which is not centered within the debond region (topmost arrow). The stress magnitude of the bow-tie pattern is similar to the bond front stress, indicating the particle is carrying significant load, but because it is not centered, it is expected that significant gas pressure is present as well. Previously, the only method of determining if this type of defect was particle supported was to place the sample in a pressure chamber and monitor the change in the fringe order of Newton's rings as the external pressure was varied.[17]

Finally, the large defect near the top left of Fig. 4 illustrates the difficulty in measuring the full extents of trapped-gas defects. As mentioned previously, the edge of the last detectable Newton's ring in the IRT images does not correspond the full extent of the debond region. The defect opening displacement field transitions from a maximum at the center to zero at the defect boundary, creating a gradual shift in optical intensity for a subfringe defect. As a result, the bond front location is not easily discernable with IRT imaging. For debonds that are perfectly circular, a closed form analytical solution can be used to approximate the debond radius as long as one can accurately measure the height of the debond and the edge of the last Newton's ring.[18] However, many of the debond

regions shown in these images are not circular. A further complication with this technique is found in the large debond region on the left side of Fig. 4(a), which displays very symmetric Newton's rings whereas Fig. 4(c) shows that the actual debond front is not nearly as symmetric. As Fig. 4(b) shows, IR-GFP imaging can more accurately locate trapped defect boundaries by locating the circumferential region of highest stress field.

3.1.2 *Results for single-side-polished wafers*

A series of anodically bonded samples utilizing P-doped (100) single-side-polished silicon substrates, 525 μm thick, were fabricated with the same Pyrex substrates described previously. The polished surface of silicon was utilized for bonding purposes. Figure 5(a) shows a typical IRT image of a representative sample, with a large region of slightly darker optical density near the lower right corner. A full set of Newton's rings does not form, indicating that even though the in-plane extents of this debond are nearly identical to the large defect in Fig. 4(a), the opening displacement is less. Two other regions with a change in optical density are visible above this large defect, but they are quite difficult to discern from the background contrast associated with wafer roughness. The rough surface pattern

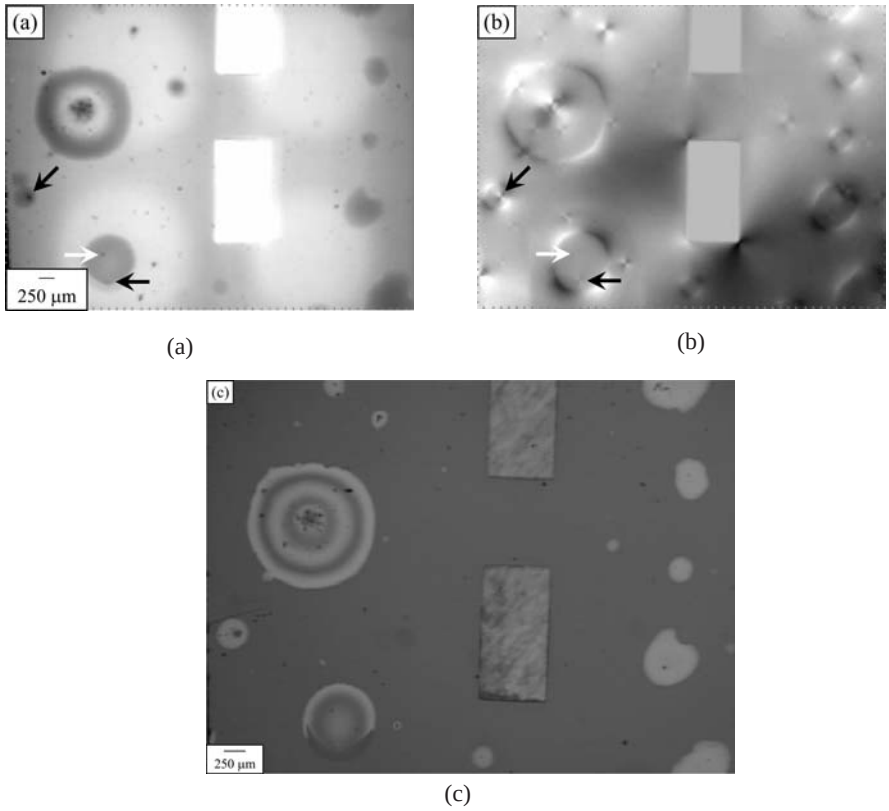

Fig. 4. Anodically bonded sample populated with trapped gas bubbles and particles. (a) IRT image and (b) shear stress image from IR-GFP; (c) visible-light reflection microscopy image. The square features visible in these images are due to windows etched in the silicon die for a separate investigation.

confounds the images in Fig. 5(a) compared with the relatively clean image in Fig. 4(a), illustrating the difficulty in locating defects when the outer surface is not polished. By viewing only the IRT image, the remainder of this bonded sample would be deemed defect free.

The shear stress image in Fig. 5(b), however, shows multiple trapped gas bubble and particle signatures distributed throughout the entire image. Imaging by visible-light microscopy, Fig. 5(c), confirms that each of the signatures identified using the IR-GFP corresponds to an interfacial defect. The large debond appears to be only slightly supported by a trapped particle near its center, as there is only a very modest contact stress signature in the IR-GFP image. Compared with the double-side-polished wafers, it is difficult to differentiate between trapped particle and trapped gas defects in Fig. 5(b), although it is possible when viewing this image in a larger format.

3.2 *Fusion bonded Silicon-Silicon samples*

Following visible-light confirmation of the characteristic defect signatures using the IR-GFP, silicon-silicon wafers were fabricated and imaged. The bonding surface was prepared using modified RCA-1 and standard RCA-2 cleaning procedures.[19] Wafers were placed in the modified RCA-1 solution (100 ml DI: 10 ml H_2O_2: 1 ml NH_4OH) on a hot plate at 73°C for 15 min and the solution was then subjected to an ultrasonic bath for 5 min. Next, the wafers were immersed for 15 min in a standard RCA-2 clean solution heated to 73°C. The wafers were then carefully rinsed with DI several times and blow dried with filtered nitrogen.

A wafer was placed in the EVG501 bond chuck with three thin spacers "flags" placed around the outer periphery. A second wafer was aligned to the first with the wafer flats. The substrates were then pressed together in the middle and the spacers removed to force bond initiation from the center of the sample. Bonding was carried out at room temperature and atmospheric pressure in a class 100 cleanroom. After bonding, each wafer pair was inspected using both IRT and the IR-GFP. A few bonded wafer pairs were then annealed in a quartz tube furnace and inspected at regular intervals to track time-dependent evolution of interfacial defects. These experiments were also carried out using both single-side- and double-side-polished wafers.

3.2.1 *Results for double side polished wafers*

In Fig. 6(a), IRT imaging of a typical fusion-bonded sample reveals two small defects, indicated by the black arrows. These trapped defects are too small to be located with wafer-scale IRT imaging, but can be detected at this magnification level, even though the opening profiles are too thin to produce a set of Newton's rings. In dramatic contrast, the shear stress image in Fig. 6(b) shows that this sample is densely populated with multiple defects. Several trapped particle and gas defects can be discerned across the entire image. As with the anodically bonded samples, the residual stress field associated with the defects allows ready differentiation between the trapped particles (black arrows), trapped-gas defects (white arrows), and artificially introduced surface contamination (outlined arrows). Both of the trapped-particle locations exhibit the signature "bow-tie" patterns identified earlier, and the trapped-gas defects show their associated ringlike signature. The topmost particle

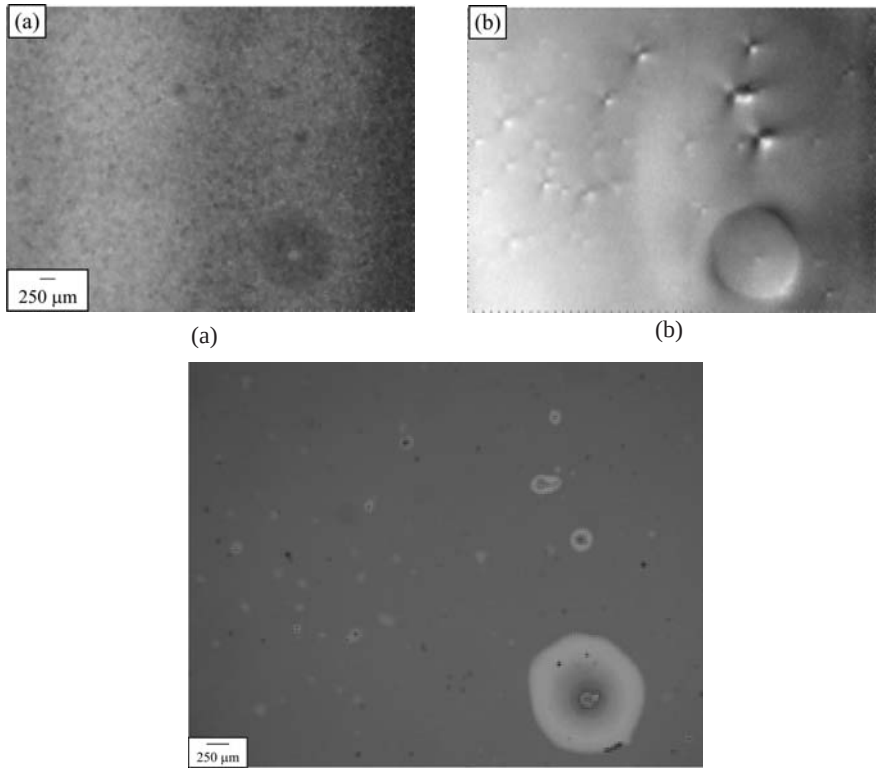

Fig. 5. Anodically bonded sample using single-side-polished silicon wafer. Trapped particles and gas bubbles are visible. (a) IRT image and (b) shear stress image from IR-GFP; (c) visible-light reflection microscopy image.

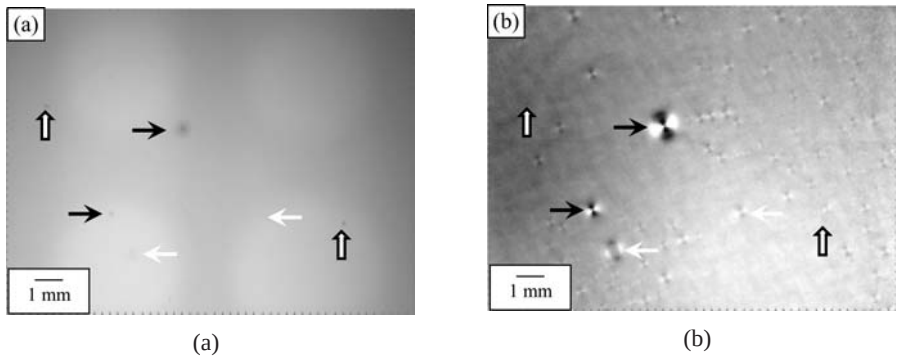

Fig. 6. IR-GFP images of double-side-polished fusion bonded-wafers; (a) IRT image, (b) shear stress image (from ref. 4).

is just large enough to be located in Fig. 6(a), while it would be difficult to reliably locate the lower defect by IRT imaging. Notice how similar this defect appears in the IRT image to that indicated by the outlined arrow, which is due to surface contamination introduced on the outer wafer surface. The IR-GFP can easily discern these defects because surface contamination does not induce residual stress in the bonded pair. The trapped gas bubble located by the lower white arrow can be discerned in the IRT image with significant eye strain, while it was not possible to detect the topmost bubble by IRT imaging. However, all of these defects are easily discerned in the IR-GFP shear stress image and many more that are too small to identify by IRT imaging. Most of the defects located in this image are a result of trapped gas bubbles as indicated by the lack of a stress concentration at the center of the defects.

In all fusion-bonded pairs, a great many microscale defects were found throughout the interface. Figure 7 shows images of a region that would be deemed defectfree using IRT imaging. When imaging the stress patterns using the IR-GFP, however, it is easily seen that this sample is densely populated with defects. In this particular case, all of the defects in this field of view are of the trapped-gas type, and measure anywhere from 300 μm to less than 50 μm in diameter. It is not uncommon for the ratio of debond radius to height to be on the order of 10^4, indicating that these small debonds would not generate a measurable interference pattern using IRT imaging. As such, the defects detected by the IR-GFP are much smaller than the dimensional threshold of IRT detection. A small optical density shift is noted at the center at Fig. 7(a), which is due to an intentionally introduced particle on the outer surface of the bonded pair. As in Figs. 3(b) and 6(b), this surface contamination does not generate a residual stress pattern in Fig. 7(b) and is thus rejected by the IR-GFP.

While bonding these samples, wafer spacing "flags" were utilized with a central contacting point to initiate a single bond front from the middle of the sample. However, these images show that despite the lack of macroscale trapped gasses, gasses are indeed trapped on a smaller scale. This phenomenon may be attributed to the nanoscale surface waviness previously discussed in the literature.[20] Even though a single bond front is initiated at a central location, this small-scale roughness may locally generate multiple bond fronts, trapping gasses on a smaller length scale. Due to its pixel resolution, wafer-level IRT imaging could not possibly locate these microbubbles. Therefore, previous investigations into time-dependent bubbles initiation may have been unable to detect an important mechanism responsible for initiating these defects.

3.2.2 *Results for single-side-polished wafers*

In a separate experiment, two single-side-polished silicon substrates were bonded on the polished faces, presenting the most difficult inspection task for IRT imaging. Figure 8(a) shows a region of the sample with a large set of Newton's rings defects as well as a few other smaller trapped defects. As noted previously,[4] in nearly all Newton's rings that would be visible with wafer-scale IRT imaging, multiple small particles are trapped in close proximity, resulting in a single very large debond area. This is nicely shown in the IR-GFP image, Fig. 8(b), where four particles (noted by black arrows) are contained within the large defect. The IR-GFP detects these particles by the presence of the unique contact

stress signature. As shown by the white arrows in both images, very small trapped gas bubbles are identified by the IR-GFP that can only be retrospectively located in the IRT image by finding the slight optical intensity shift that is visible at higher magnifications. It is also apparent from Fig. 8 that as the in-plane extents of the trapped bubbles become smaller, they become much more difficult to detect in Fig. 8(a), yet they are clearly located in Fig. 8(b). Without *a priori* location of these defects from the IR-GFP image, it would be nearly impossible to detect these trapped gas bubbles in the IRT image.

4. Tracking Defect Evolution during Anneling of Fusion-Bonded Samples

The bonded sample shown in Fig. 7 was placed in a quartz tube furnace at 500°C while flowing 5 standard liters per minute (SLM) of nitrogen. The annealing process was interrupted after 0.5, 1.0, 2.5, 5, 10, 20, 40, 60, and 80 h to inspect the defect population using the IR-GFP. Inspection times lasted anywhere from 30 min to 2 h. The sample was inspected at two locations, although images from only one location will be discussed in

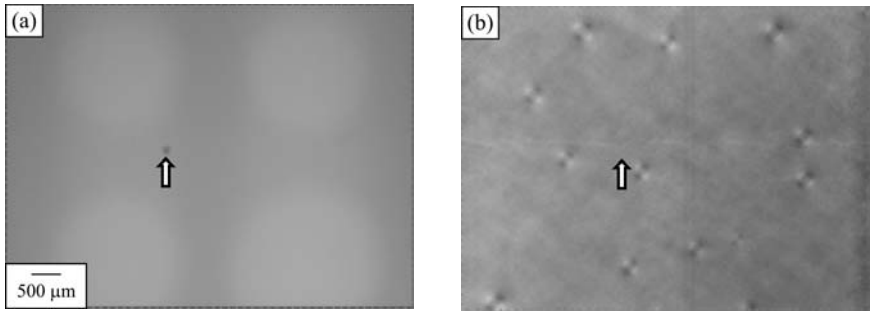

(a) (b)

Fig. 7. IR-GFP images from 'defect free' area of double-side-polished fusion-bonded wafers; (a) IRT image, (b) shear stress image.

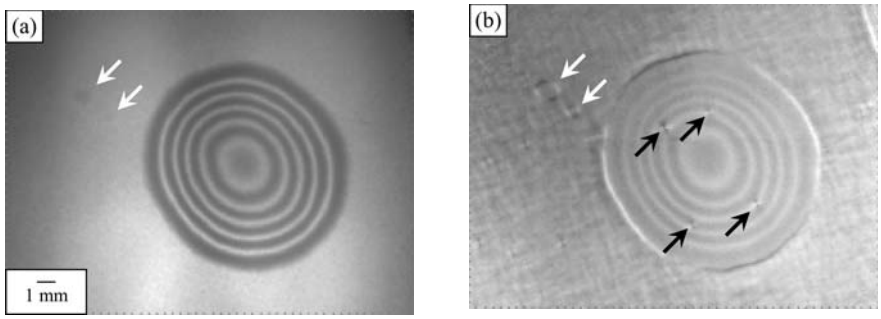

(a) (b)

Fig. 8. IR-GFP images of fusion-bonded single-side-polished wafers reveal a large defect surrounded by several smaller trapped bubbles; (a) IRT image, (b) shear stress image.

detail. Although alignment fixtures were used to locate the wafer flats, the sample was not placed in the identical position for each image. The total misalignment between each image is estimated to be approximately 0.5 mm or less in both in-plane directions.

Figures 9(a)–9(f) show the evolution of trapped-gas defects using IRT imaging, while Figs. 9(A)–9(F) show corresponding locations using IR-GFP imaging. Prior to annealing, the IRT image (Fig. 9(a)) suggests that this bonded wafer pair is defect free, while the IR-GFP image (Fig. 9(A)) again shows several trapped gas bubbles that measure approximately 100–500 μm in diameter. After annealing the sample for 30 min, distinct morphological changes in the defect distribution are detected by the IR-GFP, Fig. 9(B). The size and number of trapped gas bubbles increased noticeably from Fig. 9(A)[ii] as well as the residual stress magnitude (all images are presented on the same stress scale). The lower left portion of Fig. 9(B) shows a unique interaction between the bubbles, indicating the onset of bubble coalescence. Figure 9(b) does not display the marked changes detected by the shear stress images of the IR-GFP, although some distributed bubbles, not large enough to produce a full set of Newton's rings, are faintly visible in this image. After an additional half hour of annealing, the IRT image in Fig. 9(c) again appears the same, while the stress pattern imaging shows even more interaction among defects in the lower left corner. After 2.5 h of annealing large bubbles have formed in the lower left corner of the IR-GFP image (Fig. 9(D)), and these defects are now easily visible in the IRT image (Fig. 9(d)). The large bubbles appear to have gettered smaller ones and grown to a sufficiently large opening to generate easily noticeable interference patterns.

After 5 h of annealing, Figs. 9(e) and 9(E), two large bubbles begin to dominate the field of view. The two bubbles seen after 2.5 h of annealing appear to have merged, and the bubble just to the left of the field of view (stress field just detectable in Fig. 9(D)) has consumed other bubbles. The larger defect now has enough opening displacement to produce a full set of Newton's rings in Fig. 9(e), while the remainder of the image appears free from defects. However, the IR-GFP image in Fig. 9(E) shows that other small bubbles are still present; it also shows that few such defects exist near the large bubbles. The shear stress images, again, show that the true extents of the debond region are not the smooth edges of the fringe patterns measured by IRT, but are rather than the jagged ones. As noted in the anodically bonded samples, the presence of smooth Newton's rings does not necessarily indicate the bond front is likewise smooth and symmetrical.

After 10 h of annealing, the gas bubbles have grown to cover nearly the entire field of view (Figs. 9(f) and 9(F)), and these defects are now large enough to produce several Newton's rings. Few other defects can be seen in the IR-GFP images, even at lower magnification. From 10 h through 80 h of annealing, few changes are found in terms of the size and shape of the trapped bubbles. Several investigators have reported that these bubbles eventually recede,[5,9] a progression that was not found in these experiments. It is likely that the annealing process was not carried out for a sufficiently long time or that interruption of the annealing process for observation inhibited the receding process.

The maximum value of the shear stress measured at both inspection locations using the IR-GFP is plotted as a function of annealing time in Fig. 10. These values were calculated directly from the images presented in Fig. 9 using eq. (1) and the stress-optic coefficient for this sample inspected with the [110] direction oriented horizontally.[21] Assuming a potential

[ii]It was not possible to directly track the evolution of individual bubbles because too much time elapsed between the image captures. In-situ experiments are being planned to allow individual bubble tracking.

misalignment of 5°, the coefficient used for this data set is $C = 7.07 \pm 0.15 \times 10^{-12}$ Pa^{-1}. The only other information that must be known prior to obtaining quantitative results is the thickness of the sample, which is well controlled with modern processing techniques. Details on extracting quantitative shear stress values from these maps can be found in refs. 10 and 16. Recall that the photoelastic method integrates the shear stress through the sample thickness, so these values are actually a through-thickness integrated value. During the first 10 h of annealing, the maximum stress rose steadily, from just below 3 MPa to nearly 6 MPa at the first inspection location, reaching nearly 8 MPa at the second location. For both locations, the maximum stress was measured after 10 h of annealing. Beyond 10 h, the maximum stresses drops to a lower value. At the second inspection location, the maximum stress dropped sharply after 10 h of annealing, only to recover to approximately 7 MPa after 60 h of annealing. Data collection is highly repeatable, so the total uncertainty, which also takes into account the potential misalignment of the sample during inspection, is estimated as ±5%.

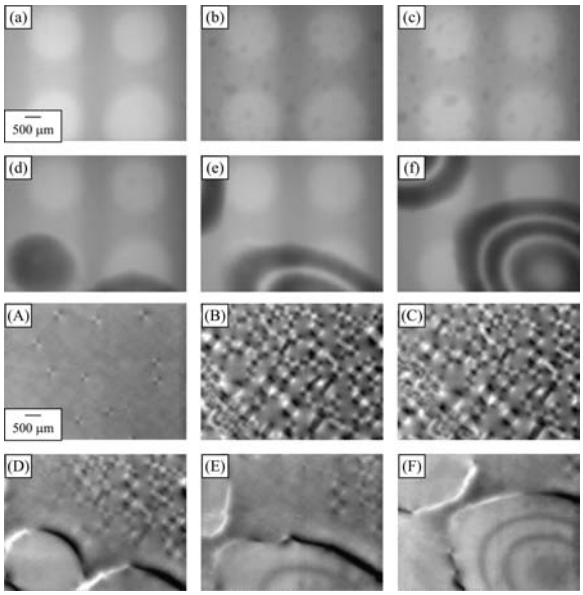

Fig. 9. IR-GFP images of annealed fusion-bonded double-side-polished wafers; IRT image (a) prior to annealing, and after (b) 0.5 h, (c) 1.0 h, (d) 2.5 h, (e) 5.0 h, (f) 10 h, and (A–F) associated shear stress images.

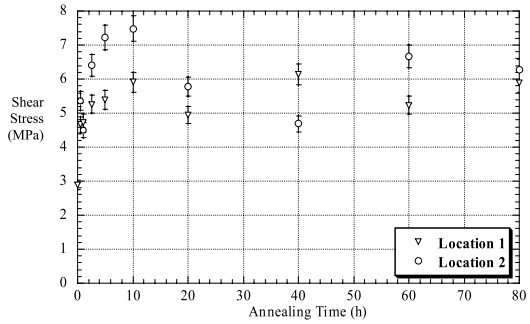

Fig. 10. Maximum integrated shear stress measured using IR-GFP as a function of annealing time for double-side-polished fusion-bonded silicon-silicon sample.

5. Conclusions

A method of locating and classifying defects in bonded semiconductors was introduced. Subfringe debonds, too thin to produce the Newton's rings associated with conventional infrared transmission (IRT) imaging, are readily detected using an infrared grey-field polariscope (IR-GFP). The IR-GFP was validated by first inspecting anodically bonded glass-silicon samples, where the defect population could be verified using high-magnification visible-light reflection microscopy. The largest defects were detected by conventional IRT imaging, but a large population of small defects could only be found using IR-GFP imaging. Furthermore, the residual stress patterns associated with trapped-particle and trapped-gas defects are easily differentiated using the IR-GFP. Gasses trapped during anodic and fusion bonding are found to have residual stresses of the same order as the contact stresses associated with trapped particles. Single-side-polished wafers, which are notoriously difficult to inspect by IRT imaging, were successfully examined with the IR-GFP.

An initial investigation of time-dependent bubble growth during annealing was carried out using IR-GFP imaging. These experiments indicate that large populations of trapped-gas defects with diameters on the order of 100 μm are present prior to annealing. Earlier studies that described the appearance of time-dependent bubbles would not have detected this preexisting defect population that may be responsible for bubble initiation. As early as 30 min into the annealing process, the stress interactions in certain regions indicated locations that later formed macroscale bubbles. With continued annealing, these bubbles coalesce into larger defects that become visible using conventional IRT imaging. In addition to improved defect resolution, the IR-GFP permits quantitative measurement of the residual stress in defects, and enables quantification of the evolution of stress with annealing.

Acknowledgemtnt

The authors greatfully acknowledge funding from the National Science Foundation through a Small Business Technology Transfer grant #0319448.

References

1 Q. -Y. Tong and U. Gösele: Semiconductor Wafer Bonding, Science and Technology (Wiley & Sons, New York, 1999).
2 T. R. Anthony: J. Appl. Phys. **58** (1985) 1240.
3 C. Harendt, H. G. Graf, E. Peneteker and B. Hofflinger: Sens. Actuators, A **23** (1990) 927.
4 G. Horn, T. Mackin and J. Lesniak: Exp. Mech. **45** (2005) 457.
5 M. Shimbo, K. Furukawa, K. Fukuda and K. Tanzawa: J. Appl. Phys. **60** (1986) 2987.
6 T. Abe, M. Nakano, T. Itho, T. Takei, A. Uchiyama, K. Yoshizawa and Y. Nakazato: Proc. Conf. on Solid State Devices and Materials (1990) 853.
7 K. Mitani, V. Lehmann, R. Stengl, D. Feijoo, U. Gösele and H. Massoud: Jpn. J. Appl. Phys. **30** (1991) 615.
8 S. Mack, H. Baumann, U. Gösele, H. Werner and R. Schlögl: J. Electrochem. Soc. **144** (1997) 1106.
9 A. Ayón, X. Zhang, K. Turner, D. Choi, B. Miller, S. Nagle and S. M. Spearing: Sens. Actuators, A **103** (2003) 1.
10 G. Horn, J. Lesniak, T. Mackin and B. Boyce: Rev. Sci. Instrum. **74** (2005) 45108.
11 G. Horn, J. Lesniak, T. Mackin and B. Boyce: Exp. Tech. **28** (2004) 19.
12 M. A. Schmidt: Proc. IEEE **86** (1998) 1575.
13 J. Lesniak, M. J. Zickel, D. J. Trate, R. Lebrecque and K. Harkins: Proc. SEM Spring Conf. on Experimental Mechanics (SEM, Cincinnati, 1999) 860.
14 J. R. Lesniak, M. J. Zickel, C. S. Welch and D. F. Johnson: Proc. SEM Spring Conf. on Experimental Mechanics (SEM, Bellevue, 1997) 219.
15 D. B. Marshall and B. R. Lawn: J. Mater. Sci. **14** (1979) 2001.
16 G. Horn: Ph.D. Dissertation, University of Illinois at Urbana-Champaign (2004).
17 K. Wan, R. Horn, S. Courmont and B. Lawn: J. Mater. Res. **8** (1993) 1128.
18 D. Pasquariello and K. Hjort: J. Electrochem. Soc. **147** (2000) 2343.
19 W. Kern: Handbook of Semiconductor Wafer Cleaning Technology (Noyes Publications, New Jersey, 1993).
20 W. P. Maszara, B. L. Jiang, A. Yamada, G. A. Rozgonyi, H. Baumgart and A. J. R. de Kock: J. Appl. Phys. **69** (1991) 257.
21 T. Zheng and S. Danyluk: J. Mater. Res. **17**X (2002) 36.